Artificial Force Field for Haptic Feedback in UAV Teleoperation

Thanh Mung Lam, Harmen Wigert Boschloo, Max Mulder, and Marinus M. van Paassen, *Member, IEEE*

***Abstract*—The feedback upon which operators in teleoperation tasks base their control actions differs substantially from the feedback to the driver of a vehicle. On the one hand, there is often a lack of sensory information; on the other hand, there is additional status information presented via the visual channel. Haptic feedback could be used to unload the visual channel and to compensate for the lack of feedback in other modalities. For collision avoidance, haptic feedback could provide repulsive forces via the control inceptor. Haptic feedback allows operators to interpret the repulsive forces as impedance to their control deflections when a potential for collision exists. Haptic information can be generated from an artificial force field (AFF) that maps environment constraints to repulsive forces. This paper describes the design and theoretical evaluation of a novel AFF, i.e., the parametric risk field, for teleoperation of an uninhabited aerial vehicle (UAV). The field allows adjustments of the size, shape, and force gradient by means of parameter settings, which determine the sensitivity of the field. Computer simulations were conducted to evaluate the effectiveness of the field for collision avoidance for various parameter settings. Results indicate that the novel AFF more effectively performs the collision avoidance function than potential fields known from literature. Because of its smaller size, the field yields lower repulsive forces, results in less force cancellation effects, and allows for larger UAV velocities. This indicates less operator control demand and more effective UAV operations, both expected to lead to lower operator workload, while, at the same time, increasing safety.**

***Index Terms*—Artificial force field (AFF), collision avoidance, haptic feedback, teleoperation, uninhabited aerial vehicle (UAV).**

I. Introduction

TELEOPERATION of an uninhabited aerial vehicle (UAV) can be difficult due to poor situation awareness [1], [2]. Tactile, auditory, and motion cues are usually absent. Principal information transfer is by means of visual information, provided by a camera on board the remote vehicle. The information is often limited due to poor camera resolution and restricted field of view (FOV) [1]–[3]. Moreover, while hovering a UAV helicopter, i.e., the vehicle in our study, the camera may not always point in the direction of motion. Operators cannot perceive obstacles outside the FOV, which could potentially lead to dangerous situations, including collisions.

Teleoperation performance and efficiency may be improved by providing additional information, e.g., in terms of external forces through a haptic control device [4]–[8]. Haptic feedback would allow the operator to directly perceive the information about the environment through the sense of touch. Using haptic feedback for a collision avoidance system (CAS) requires an algorithm to generate artificial forces on the control inceptor in order for the operator to perceive through the haptic channel, information about the environment before actual contact with an obstacle occurs. Care must be taken when using force feedback, however, since both the magnitude of the repulsive forces and also the mapping algorithm affect operator performance and workload [9], [10].

A starting point for the design of artificial forces is formed by artificial force fields (AFFs), such as used for local path planning in autonomous ground vehicles and robots [11]–[17]. Known problems with these fields are the difficult passage through narrow corridors and the occurrence of local minima in the field that could result in a robot getting trapped. Research on autonomous robot navigation led to various solutions for generating AFFs that overcome these problems [18]–[22]. Some suggested abandoning the use of AFFs altogether and proposing the use of obstacle-presence probabilities to select a steering direction along a collision-free path [23], [24].

In the manual teleoperation of a UAV, however, local minima in the AFF are less of concern. These can be overruled by the human operator, based on, for instance, the visual displays that usually complement the haptic feedback, simply guiding the UAV to a destination. It is more important to consider the effects of the force field on the manual control of vehicle motion in an obstacle-laden environment. In other words, can the information from the AFF be used effectively for haptic feedback to the human operator, without causing oscillatory vehicle motion or higher operator workload? Furthermore, for a UAV helicopter, the dynamics and its degrees of freedom play an important role. Whereas a ground vehicle can be stopped immediately when oscillations or control difficulties occur, this is often impossible for a helicopter, and loss of stable control may rapidly cause it to crash.

The overall goal of our research project is to develop a CAS in the teleoperation of a UAV helicopter, using haptic feedback on the operator control manipulator. It is assumed that the CAS complements a visual interface that consists of, among others,

Manuscript received November 8, 2007; revised August 15, 2008. First published September 25, 2009; current version published October 16, 2009. This work was supported by the Netherlands Agency for Aerospace Programmes (NIVR) under NIVR Project 49307TU. This paper was recommended by Associate Editor N. Sarter.

T. M. Lam is with the Control and Simulation Division, Faculty of Aerospace Engineering, Delft University of Technology (TU Delft), 2629 HS Delft, The Netherlands, and also with Moog, 2150 AD Nieuw-Vennep, The Netherlands (e-mail: mung.lam@gmail.com).

H. W. Boschloo is with the Aerospace Software and Technologies Institute, Delft University of Technology, 2629 HG Delft, The Netherlands (e-mail: h.w.boschloo@tudelft.nl).

M. Mulder and M. M. van Paassen are with the Control and Simulation Division, Faculty of Aerospace Engineering, Delft University of Technology (TU Delft), 2629 HS Delft, The Netherlands (e-mail: m.mulder@tudelft.nl; m.m.vanpaassen@tudelft.nl).

Digital Object Identifier 10.1109/TSMCA.2009.2028239

a display showing an outside-world image as seen by a camera mounted on the vehicle. Haptic feedback is designed in two stages. The first stage concerns the calculation of a feedback signal on the basis of the motions of the UAV with respect to the environment. In the second stage, the control inceptor and the haptic interface are designed [25].

This paper concentrates on the first stage, i.e., the development of an AFF that maps environmental constraints to forces on the control device. In this mapping, it is hypothesized that the environment is static, i.e., contains no moving objects other than the UAV helicopter, and can be detected by a simulated sensor. At this stage of the project, the following is further assumed: 1) The helicopter only moves in the horizontal plane; 2) the UAV dynamics are those of a control-augmented "pilot-friendly" helicopter [26]; and 3) the dynamics are identical in every direction, with a constant deceleration limit. Furthermore, the effects of transmission delays that are common in teleoperation are neglected; these are treated in detail in our prior work [27], [28].

The structure of this paper is as follows. First, a review on some AFFs, well known from literature, will be given. These fields serve as a basis for the discussion of new AFFs. Second, a set of candidate fields will be evaluated in the closed-loop offline computer simulations. Third, results of a sensitivity study that investigated the effects of some of the main AFF parameters on CAS performance will be discussed. This paper ends with a discussion of the main results and limitations of this study, recommendations for further research, and conclusions.

II. AFFs

The purpose of an AFF, also referred to as "potential field" in the literature, is to map environment constraints to imaginary forces, acting on a vehicle. Whereas obstacles are mapped to repulsive forces, a target destination can be mapped to an attractive force. A repulsive force from an obstacle is generated by taking the gradient of the potential field. The sum of the forces from each individual obstacle results in the final repulsive force vector, containing the direction and magnitude for steering the vehicle. This would lead to a collision-free path toward a target [14], [16].

In the teleoperation of a UAV helicopter, the repulsive forces from the obstacles can be used for a CAS using haptic feedback on the operator control device. No haptic information of the target destination would be required because, in this application, it is the human operator who determines where to go based on the visual information, e.g., from a camera image or from a navigation display.

Next, some common AFFs that have been developed for robots and ground vehicles will be introduced, followed by the description of two newly developed AFFs for haptic feedback.

A. GPF

Khatib [13] suggested the use of an artificial potential field for collision avoidance that was based on the distance between a robot arm and an object. The repulsive force from the object can be calculated by taking the gradient of this potential field.

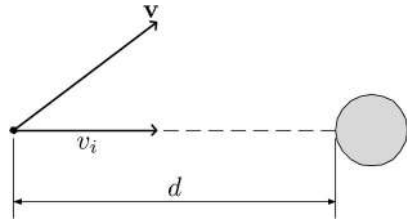

Fig. 1. GPF requires both the distance d to an obstacle and the velocity component v_i (of the velocity vector $\mathbf{v}$) toward this obstacle.

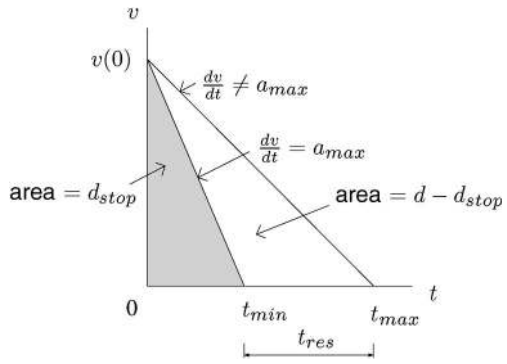

Fig. 2. Definition of $t_{\min}$, $t_{\max}$, t_{res}, and d_{stop} adopted from [14].

Due to the fact that the algorithm only considered the distance between the robot and the object, repulsive forces would always be generated also when the robot did not move toward or even when moving away from the object. For the teleoperation of a UAV helicopter, this property makes this field less suitable. For example, during a hover maneuver near an object, the operator would be forced to continuously counteract the repulsive forces from the control device, which would lead to an increase in the physical workload. Additionally, the algorithm requires an analytical description of the objects by composition of primitives, which would not be practical in environments with complex or unknown objects [29].

Krogh [14] extended the concept of artificial potential fields by including the relative velocity of the vehicle with respect to an obstacle (see Fig. 1). The inclusion of relative velocity prevents the potential field from generating repulsive forces when the vehicle is near an obstacle but, at the same time, not moving toward it. In addition, this formulation can take the vehicle deceleration limits into account. These features result in the so-called generalized potential field (GPF).

The GPF is based on calculating the time during which a vehicle has to be accelerated (or decelerated) to avoid an obstacle. The GPF is then obtained by taking the inverse of the difference between the *maximum* $(t_{\max})$ and *minimum avoidance time* $(t_{\min})$, which is the *reserve avoidance time* (t_{res}) (see Fig. 2). The *minimum avoidance time* is the minimum time in which v_i can be decreased to zero, using the vehicle maximum deceleration $a_{\max}$ in the direction of the obstacle

$$t_{\min} = \frac{v_i}{a_{\max}}. \tag{1}$$

The *maximum avoidance time* is defined as the time in which the nonzero velocity v_i toward an obstacle decreases to zero when a constant deceleration that is less than the maximum

deceleration is applied. Then, $t_{\max}$ can be described as a function of the distance from an obstacle d and the current velocity component toward the obstacle v_i

$$t_{\max} = \frac{2d}{v_i}. \tag{2}$$

Using (2) and (1), the GPF is described as

$$P(d, v_i) = \begin{cases} 0, & \text{for } v_i \leq 0 \\ \frac{1}{t_{\max} - t_{\min}} = \frac{a_{\max} v_i}{2da_{\max} - v_i^2}, & \text{for } v_i > 0. \end{cases} \tag{3}$$

The gradient of this potential field with respect to distance d provides an avoidance vector, giving the direction of acceleration to avoid collision. The magnitude of this gradient represents the level of urgency of accelerating away from the obstacle.

Later, Khatib and others included the velocity and deceleration limits into their potential field [30]–[32].

B. BRF

The GPF described previously has several properties that make it less suitable for haptic feedback. First, as the *reserve avoidance time* approaches zero, the potential field value approaches infinity, which results in an avoidance vector of infinity. This would occur when the maximum deceleration is being used. However, the infinite avoidance vector is not suitable for practical use due to hardware limitations and restrictions on applying force feedback to human operators. A straightforward solution to this problem would be to limit the values of the potential field to an upper boundary, resulting in the following description of the potential function:

$$P_t(d, v_i) = \begin{cases} 0, & v_i \leq 0 \\ 1, & t_{\text{res}}(d, v_i) \leq G \\ G\frac{1}{t_{\text{res}}(d, v_i)}, & t_{\text{res}}(d, v_i) > G \end{cases} \tag{4}$$

with $t_{\text{res}}(d, v_i)$ being the reserve avoidance time as a function of the distance d and velocity v_i with respect to an obstacle. A positive gain G can be used to scale the function and adjust the field sensitivity. Consider the potential value to be dimensionless; then, G has a time unit and can be interpreted as a time factor causing the field size to increase or reduce in the moving direction.

A small G results in a small field which is less sensitive. The UAV then would be able to approach an object more closely before repulsive forces are perceived. A large G results in a large field size, a highly sensitive field where the repulsive forces would be already perceived when the UAV is still located far from the obstacles.

A schematic representation of the GPF with a limited maximum value can be found in Fig. 3. The gray area represents a "critical" area in which obstacles should not be located and where the potential value has a maximum value of one. The boundary of this area d_m is determined when the combination of the relative position and velocity causes the potential value in (4) to become one. The "protected zone" of the UAV is defined as a circle with radius r_{pz}; any obstacles within this zone means a collision, which should be prevented at all times.

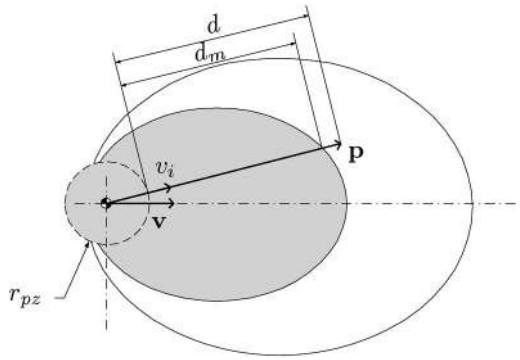

Fig. 3. Representation of the GPF with a velocity component v_i toward an obstacle $\mathbf{p}$ with limited potential value.

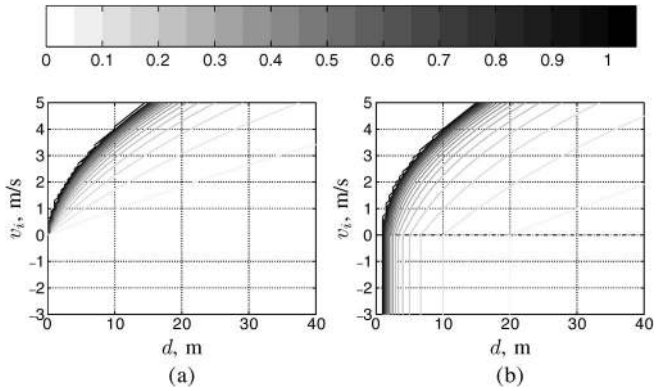

Fig. 4. One-dimensional contour plots of the potential functions using the reserve avoidance time ($a_{\max} = 1\ \text{m/s}^2, G = 1\ \text{s}$). (a) $P_t(d, v_i)$. (b) $P_{td}(d, v_i)$.

Fig. 4(a) shows the potential field as a function of the relative velocity and distance from an obstacle. Here, the potential function is zero for a zero velocity, independent of the distance. Additionally, the GPF only maps obstacles that are located in the direction of motion. Obstacles at the side or behind will hardly be "detected." For a UAV helicopter, it is crucial, however, to be aware of these obstacles due to its lateral maneuverability, particularly during hover. A possible solution to this problem is to add an extra term to the potential field that only depends on the distance toward an obstacle. In order not to obtain the disadvantageous effect that is similar to the potential field from Khatib, however, this term should only generate repulsive forces for very small distances. This results in the following modification of the potential function:

$$P_{td}(d, v_i) = \begin{cases} 1, & t_{\text{res}}(d, v_i) \leq 0 \\ 1, & \frac{1}{t_{\text{res}}(d, v_i)} + \frac{1}{d} \geq \frac{1}{G} \\ G\left(\frac{1}{t_{\text{res}}(d, v_i)} + \frac{1}{d}\right), & \text{otherwise.} \end{cases} \tag{5}$$

Fig. 4(b) shows that, for a zero and even negative velocity component (i.e., moving away from an obstacle), the potential field would result in repulsive forces at some distance from an obstacle.

When considering the distance instead of time, a new variable can be defined, the so-called *reserve avoidance distance*. It is defined as the difference between the braking distance when decelerating with less than the maximum deceleration and the minimum required braking distance corresponding to

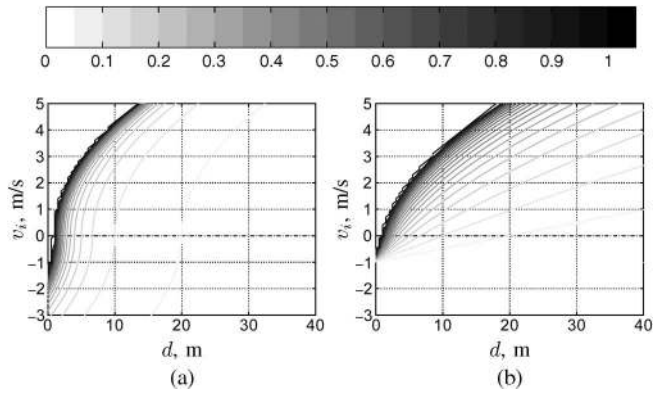

Fig. 5. One-dimensional contour plots of the potential functions using the reserve avoidance distance ($a_{\max} = 1$ m/s^2, $G = 1$ s). (a) $P_d(d, v_i)$. (b) $P_{dv}(d, v_i)$.

the maximum deceleration. The reserve avoidance distance can be described as

$$d_{\text{res}}(d, v_i) = \begin{cases} d + d_{\text{stop}}(v_i) = \frac{2a_{\max}d + v_i^2}{2a_{\max}}, & v_i \leq 0 \\ d - d_{\text{stop}}(v_i) = \frac{2a_{\max}d - v_i^2}{2a_{\max}}, & v_i > 0 \end{cases} \quad (6)$$

with positive relative velocity defined as heading toward an obstacle and negative velocity defined as moving away from an obstacle; d_{stop} represents the minimum required braking distance according to the constraint that the denominator in (3) must not be zero

$$d_{\text{stop}}(v_i) = \frac{v_i^2}{2a_{\max}}. \quad (7)$$

The minimum required braking distance is represented in Fig. 2 as the area under the line with a slope of $a_{\max}$.

Taking the inverse of the reserve avoidance distance from (6), a modified potential function can be formulated

$$P_d(d, v_i) = \begin{cases} 1, & d_{\text{res}}(d, v_i) \leq G \\ G\frac{1}{d_{\text{res}}(d, v_i)}, & d_{\text{res}}(d, v_i) > G. \end{cases} \quad (8)$$

Fig. 5(a) shows that, for a zero and even negative velocity at a relatively large distance with respect to an obstacle, the potential function will still generate repulsive forces. In order to solve for this problem, an extra term can be added which is dependent on the velocity

$$P_{dv_i}(d, v_i) = \begin{cases} 1, & \begin{cases} d_{\text{res}}(d, v_i) \leq 0 \\ \frac{1+v_i}{d_{\text{res}}(d, v_i)} \geq \frac{1}{G} \end{cases} \\ 0, & \frac{1+v_i}{d_{\text{res}}(d, v_i)} \leq 0 \\ G\left(\frac{1+v_i}{d_{\text{res}}(d, v_i)}\right), & \text{otherwise.} \end{cases} \quad (9)$$

Fig. 5(b) shows a similar plot as for the reserve avoidance time in Fig. 4(a). However, here, the potential function only generates repulsive forces for small negative velocities at small distances from an obstacle.

Equation (9) can be considered as a new potential field, based on the theory of the GPF. The novel field has strength on a scale from zero to one and serves as a risk field, giving an indication about the risk of hitting an obstacle. In the following, it will be referred to as the basic risk field (BRF). The lower limit 0 represents the minimum risk; the upper limit 1 represents the maximum risk. These can be translated to a minimum and maximum force feedback, respectively, that is proportional to a gain. Fig. 6 shows the contour lines of the BRF for two velocities.

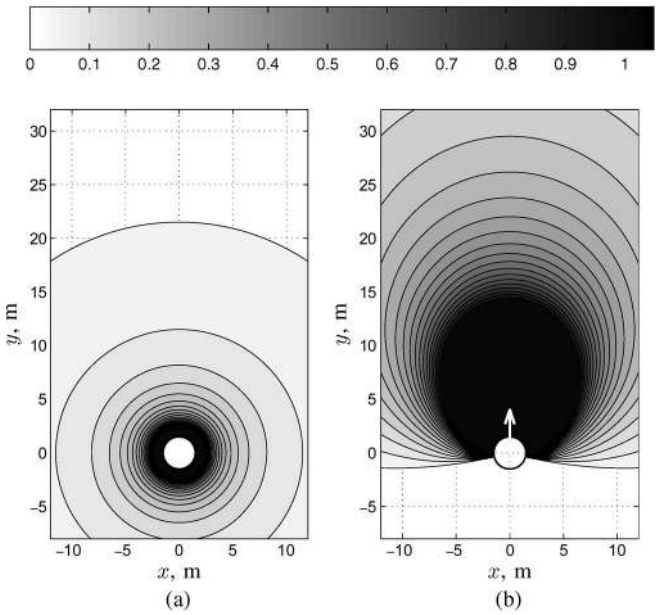

Fig. 6. Two-dimensional contour plots of the BRF for two velocities ($a_{\max} = 1$ m/s^2, $G = 1$ s). The vehicle is represented by the circular protection zone with 1.5-m radius. All coordinates within the innermost contour line correspond to the maximum risk value of one. (a) $v = 0$ m/s. (b) $v = 4$ m/s.

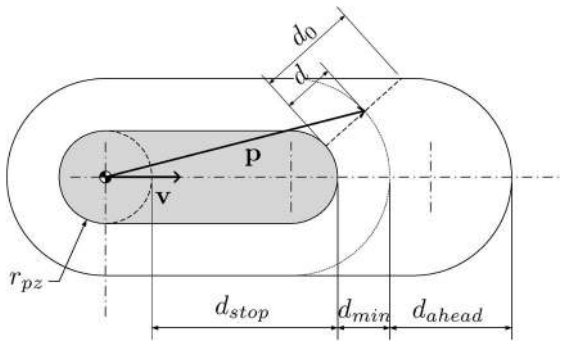

Fig. 7. Parameter and variable definitions for the PRF.

The advantage of the BRF is that the maximum value is finite and a force is calculated only for small negative velocities at small distances from an obstacle. A disadvantage is that the field becomes rather large for high velocities, which may result in control problems when moving through a narrow passage.

C. PRF

To gain more control over the size and shape of the risk field, a new field was formulated that allows parametric adjustment of its shape: the parametric risk field (PRF) [33]. This field depends on a number of parameters that determine the maximum and minimum risk boundary of the field (see Fig. 7).

The gray area represents the critical region, with a maximum risk of one, which is similar to the BRF. An obstacle is not allowed to be in this region. The length of the critical region consists of the diameter of the vehicle protection zone $2r_{\text{pz}}$ plus

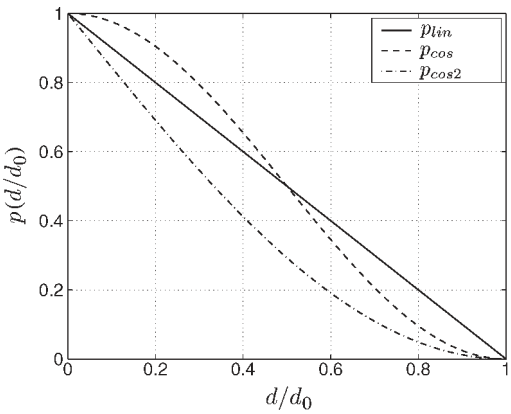

Fig. 8. Various risk functions of d/d_0.

a braking distance d_{stop}. Similar to (7), the distance d_{stop} in the direction of motion can be obtained from the velocity $\mathbf{v}$ and the maximum deceleration of the vehicle $a_{\max}$

$$d_{\text{stop}} = \frac{|\mathbf{v}|^2}{2a_{\max}}. \tag{10}$$

The outer boundary of the field is defined by a minimum distance from the critical region $d_{\min}$, but, in the direction of motion, the field is extended with d_{ahead}, which depends on $\mathbf{v}$ and the time parameter t_{ahead}

$$d_{\text{ahead}} = |\mathbf{v}| t_{\text{ahead}}. \tag{11}$$

The time parameter t_{ahead} ensures that the operator has enough time to react to obstacles in the direction of motion, particularly when flying at high speed. Outside the field, the risk is zero. The geometry of the PRF is fully described by the parameters r_{pz}, $d_{\min}$, and t_{ahead}, together with the vehicle velocity vector $\mathbf{v}$ and maximum deceleration $a_{\max}$.

To calculate the risk value at vector point $\mathbf{p}$, two variables, namely, d and d_0, are calculated as a function of $\mathbf{p}$ and $\mathbf{v}$, as shown in Fig. 7. Here, d is the shortest distance between $\mathbf{p}$ and the critical region, and d_0 is the distance between the critical region and the outer boundary of the field. The ratio d/d_0 defines the position of $\mathbf{p}$ with respect to the risk field boundaries. The risk value can be calculated using a function of d/d_0

$$P(\mathbf{p},\mathbf{v}) = \begin{cases} 0, & \text{if } \mathbf{p} \text{ outside outline} \\ 1, & \text{if } \mathbf{p} \text{ inside critical region} \\ p\left(\frac{d(\mathbf{p},\mathbf{v})}{d_0(\mathbf{p},\mathbf{v})}\right), & \text{otherwise.} \end{cases} \tag{12}$$

The risk function $p(d/d_0)$ can freely be selected as long as it is continuous and the boundary conditions $p(0) = 1$ and $p(1) = 0$ are met. Fig. 8 shows an example of a linear, a cosine, and a shifted cosine function using (13)–(15), respectively

$$p_{\text{lin}}\left(\frac{d}{d_0}\right) = 1 - \frac{d}{d_0} \tag{13}$$

$$p_{\cos}\left(\frac{d}{d_0}\right) = \frac{1}{2}\cos\left(\frac{d}{d_0}\pi\right) + \frac{1}{2} \tag{14}$$

$$p_{\cos 2}\left(\frac{d}{d_0}\right) = \cos\left(\frac{d}{d_0}\frac{\pi}{2} + \frac{\pi}{2}\right) + 1. \tag{15}$$

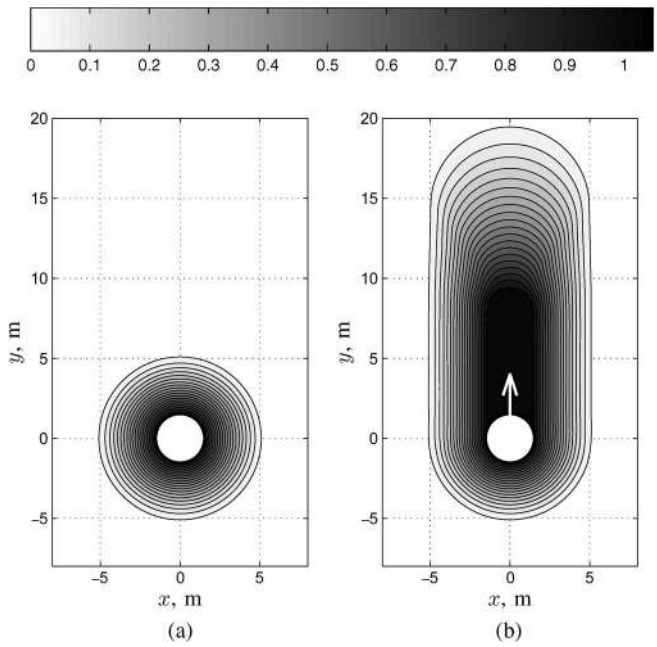

Fig. 9. Two-dimensional contour plots of the PRF for two velocities ($r_{\text{pz}} = 1.5$ m, $a_{\max} = 1$ m/s^2, $d_{\min} = 4.5$ m $(= 3r_{\text{pz}})$, and $t_{\text{ahead}} = 2$ s). (a) $v = 0$ m/s. (b) $v = 4$ m/s.

The different functions of d/d_0 result in different gradients of the risk field, and, thus, the growth of the repulsive forces when the vehicle approaches an obstacle is different.

The shifted cosine function $p_{\cos 2}$ does not have a jump in the slope at $d/d_0 = 1$ as in the case of the linear function, and, from $d/d_0 = 0.4$, the function increases almost linearly to one. The cosine function has a much larger gradient and would therefore lead to a relatively quick growth to the maximum value of one. Therefore, the shifted cosine function was chosen to be used for the PRF in this study. Fig. 9 shows the contour lines of the field for two velocities. In comparison with the BRF, illustrated in Fig. 6, the PRF is smaller, that is, for these particular parameter settings.

Summarizing, the PRF offers the ability to change the size and shape of the field simply by adjusting its parameters. The rate of change of the risk value is defined by the function of the ratio d/d_0. The field depends on the vehicle position and velocity and takes the deceleration limit into account, which is similar to the GPF.

D. Risk Direction and Summing Multiple Obstacles

According to the theory of the GPF, the final avoidance force vector can be obtained by taking the gradient of the potential field for every obstacle inside the field. This results in multiple avoidance vectors that need to be integrated into one final avoidance force vector. For the BRF and PRF, however, a different strategy can be used to obtain the final avoidance vector. The magnitude of a risk vector is simply equal to the risk value generated by the BRF and PRF, but the *direction* of the risk vector can be defined in two ways:

1) radial: The risk vector points toward the center of the vehicle [see Fig. 10(a)];
2) normal: The risk vector is mapped perpendicular to the obstacle surface [see Fig. 10(b)].

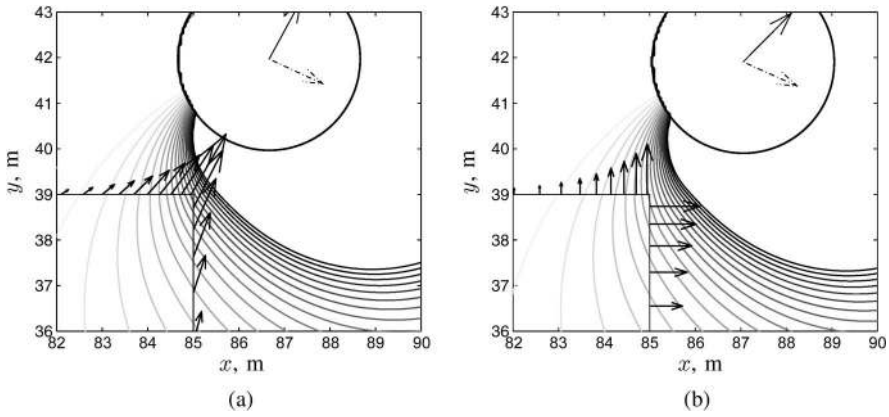

Fig. 10. Definitions of the direction of the risk vector. (a) Radial projection. (b) Normal projection.

An obstacle is detected by a discrete sensor with an angular resolution of 3°. In Fig. 10, the small arrows on the obstacle surface represent the individual risk vectors with either radial or normal projections. The resulting total risk vector is represented by the solid arrow in the center of the UAV, whereas the velocity vector is represented by the dashed-dotted arrow in the center of the UAV. For clarity, the contour surfaces are not filled.

Assuming that an obstacle is detected by discrete sensor radial lines, the individual risk vectors calculated from each sensor radial line need to be integrated into one final risk vector before transforming it into an artificial repulsive force vector acting on the vehicle. Again, there are several ways for obtaining the final avoidance risk vector:

1) sum, i.e., the sum of all risk vectors with the final avoidance vector limited to one. This method has the drawback of overestimating the final risk. For instance, although several objects at large distances are all mapped to small risk vectors, their sum may result in one large avoidance risk vector.
2) mean, i.e., the mean of all risk vectors. This method may result in an underestimated final risk. High risk values will be diminished by the low risk values.
3) max, min, i.e., the sum of the largest positive and negative risk vectors with the final avoidance vector limited to one. This method results in an avoidance vector without over- or underestimation of the final risk and was chosen to be used in this study.

The current algorithm of the BRF allows control over the size and shape of the field but is restricted by the use of only the velocity and a scale factor. The PRF allows more control of the size and shape of the risk field, which is important because these factors influence the field sensitivity and, thus, how a human operator perceives and reacts to the risk field. In the following section, the effectiveness of both AFFs will be evaluated using offline simulations with an autonomous system, flying in an obstacle-laden environment.

III. Offline Simulations

This section describes the offline simulations with an autonomous system. The simulation consisted of a simulated pilot, a UAV helicopter model, and a CAS. The CAS contains an AFF that generates repulsive forces that are fed back to the pilot. The two novel risk fields introduced previously, the BRF and the PRF, are evaluated with both normal and radial projection of the risk vectors. Several trajectories along various obstacles are used.

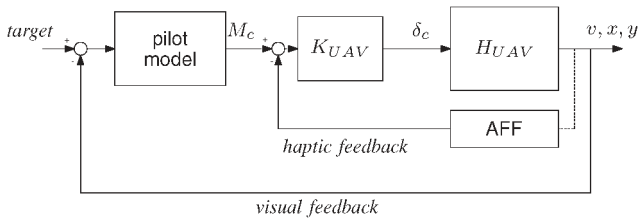

Fig. 11. Schematic representation of the closed-loop autonomous system.

A. Setup

A schematic representation of the simulation model is shown in Fig. 11. The model consisted of a visual feedback loop and a force feedback inner loop, both to the simulated pilot. The components are described next.

1) Forcing Function: The forcing function, "target" in Fig. 11, consisted of a fixed destination position that served as input to the closed-loop system.

2) Pilot: The pilot behavior was simulated by a proportional–derivative controller $(P = 0.1; D = 0.35)$ that transformed the position error of the UAV into a steering command M_c, which was then limited to 0.75.

3) UAV Helicopter: The UAV was assumed to be a user-friendly control-augmented helicopter [26], with a velocity limited to 5 m/s and a maximum acceleration/deceleration of 1 $\mathrm{m/s^2}$. The dynamics H_{UAV} between the velocity command and UAV velocity were a linear transfer function $2/(s+2)$.

4) AFF: The AFF generated the avoidance vector using the position and velocity of the helicopter and the environment constraints. The protection zone radius r_{pz} was 1.5 m. The avoidance repulsive force was proportional to the avoidance risk with a gain of one. For the simulations, the BRF was used with $G = 0.1$ s, whereas the PRF was used with $d_{\min} = 1.5$ m $(= r_{\mathrm{pz}})$ and $t_{\mathrm{ahead}} = 2$ s.

The sum of the pilot steering command and the AFF repulsive force was multiplied by $K_{\mathrm{UAV}} = 1.18$, resulting in a

steering command δ_c inserted to the UAV dynamics. Note that, when the repulsive force was larger than 0.75, the maximum steering command of the pilot, it would cause the UAV to decelerate.

A simulated sensor model that was part of the CAS was used to measure the distance between the obstacles and the UAV. The sensor had a range of 50 m and scanned 360° around the UAV with an angular resolution of 3°. Both the BRF and PRF were combined with radial and normal projection of the risk vectors, resulting in four AFF configurations.

5) Environment: Six trajectories were used that each required a specific maneuver, to investigate the effectiveness of collision avoidance and the risk of oscillatory behavior in the UAV motion, due to inherent limitations of potential fields [34]. Environment constraints along the trajectories were represented by 2-D wire-frame obstacles.

The four AFF configurations and six trajectories resulted in a total of 24 simulation conditions.

B. Hypotheses

It was hypothesized that both the BRF and PRF would result in acceptable collision avoidance. However, the BRF was expected to result in larger repulsive forces and, therefore, also smaller velocities. Additionally, the BRF was hypothesized to generate repulsive forces at a larger distance from the obstacles than the PRF and, due to its size, may result in oscillatory motions when moving through a narrow passage.

It was further hypothesized that the effects of the individual risk vectors projected normal to the obstacle surface strongly depend on the surface orientation of an obstacle. Radial risk vectors, however, always point toward the approaching vehicle. Here, the avoidance maneuver of the vehicle would mainly depend on the relative position, size, and density of the obstacles and less on the obstacles' shape.

C. Results

The results of the simulations are plotted in Fig. 12, with each trajectory marked with letters A–F. In this figure, the dotted circles represent the UAV positions, and the arrows present the total repulsive force vector, all shown with a time step of 1 s. The initial and target positions are shown with a circle (together with the letter that corresponds to the trajectory) and a "$\star$," respectively.

The results are described next for each trajectory. The most important aspects were whether the UAV collided with obstacles or the motion showed oscillatory behavior. Additionally, Fig. 13 shows the magnitude of the total risk vector, which will be used to discuss the results from a human–machine interaction perspective; Fig. 14 shows the UAV velocity.

1) Trajectory A: This trajectory involved a step change of $0.8r_{\mathrm{pz}}$ in the wall and required a 90° turn maneuver at the end of the obstacle. It was hypothesized that this scenario could lead to unstable motion near the wall [34]. The simulations, however, show no oscillatory motions for neither the BRF nor the PRF. The PRF combined with radial risk vectors, however, did result in a short oscillation after a steplike disturbance in the wall, which can be seen more clearly in Fig. 13(a).

For the PRF with normal risk vectors, there is a sudden change in direction [Fig. 12(d)] and an increase in risk near the corner at the end [Fig. 13(b)]. In practice, a close distance would result in a large risk vector magnitude, and a sudden change in the vector direction and magnitude would be noticeable for a human operator. This could lead to reflexive counteractions, which may be considered as nuisance by the human, contributing to workload.

2) Trajectory B: Here, the UAV had to move through a corridor that initially had a width of $4r_{\mathrm{pz}}$, which decreased to $2.7r_{\mathrm{pz}}$, resulting in a steplike disturbance. It was hypothesized that this disturbance could lead to oscillatory vehicle motion [34].

In the simulation, the vehicle moved in a stable manner, except for the BRF with normal projection of the risk vectors, where even a collision with the wall occurred. The BRF with radial risk vectors caused larger avoidance vectors than the PRF, which can be attributed to the larger field size [see Fig. 13(c)]. The velocity was also considerably lower with the BRF using radial projection [see Fig. 14(a)].

The PRF with normal risk vectors resulted in high fluctuations in the risk values at the step change [Fig. 13(d)]. For both risk fields, the normal risk vectors resulted in higher velocities in the narrow corridor than with radial projection [see Fig. 14(b)]. This is due to the fact that, with normal projection, the force vector component that is responsible for decelerating the UAV is strongly dependent on the obstacle surface orientation relative to the UAV motion. In this trajectory, the wall was parallel to the direction of motion, and, thus, a deceleration component did hardly emerge with the normal projection.

3) Trajectory C: Here, it was hypothesized that the vehicle would be able to stop before it hits the wall.

Fig. 12 shows that, with all fields, the UAV was indeed capable of avoiding collision by stopping in front of an object with a straight surface. The PRF generated the risk values at a closer distance to the obstacle. However, it increased faster while still yielding good collision avoidance, which indicates a more effective risk field.

4) Trajectory D: Here, the destination was blocked by a wall, and the AFF should be able to stop the UAV before the dead end.

The simulation results show that, for all AFF configurations, the UAV indeed succeeded to stop in the dead end without collision. For both radial and normal projection of the risk vector, the BRF generated the risk values in an earlier stage and increased the risk value more rapidly in the dead end than the PRF [see Fig. 13(e) and (f)]. This may lead to higher operator physical workload. The PRF resulted in a more gradual buildup of the risk vector near the dead end.

5) Trajectory E: Here, the UAV encountered two closely spaced obstacles within a distance of $3.3r_{\mathrm{pz}}$. It was expected that the vehicle would not succeed in passing between the little square object and the rectangle [34].

The simulation results show that, for all AFF configurations, the UAV successfully passed between the obstacles. Fig. 13(g) and (h) shows that the BRF generated higher risk values already

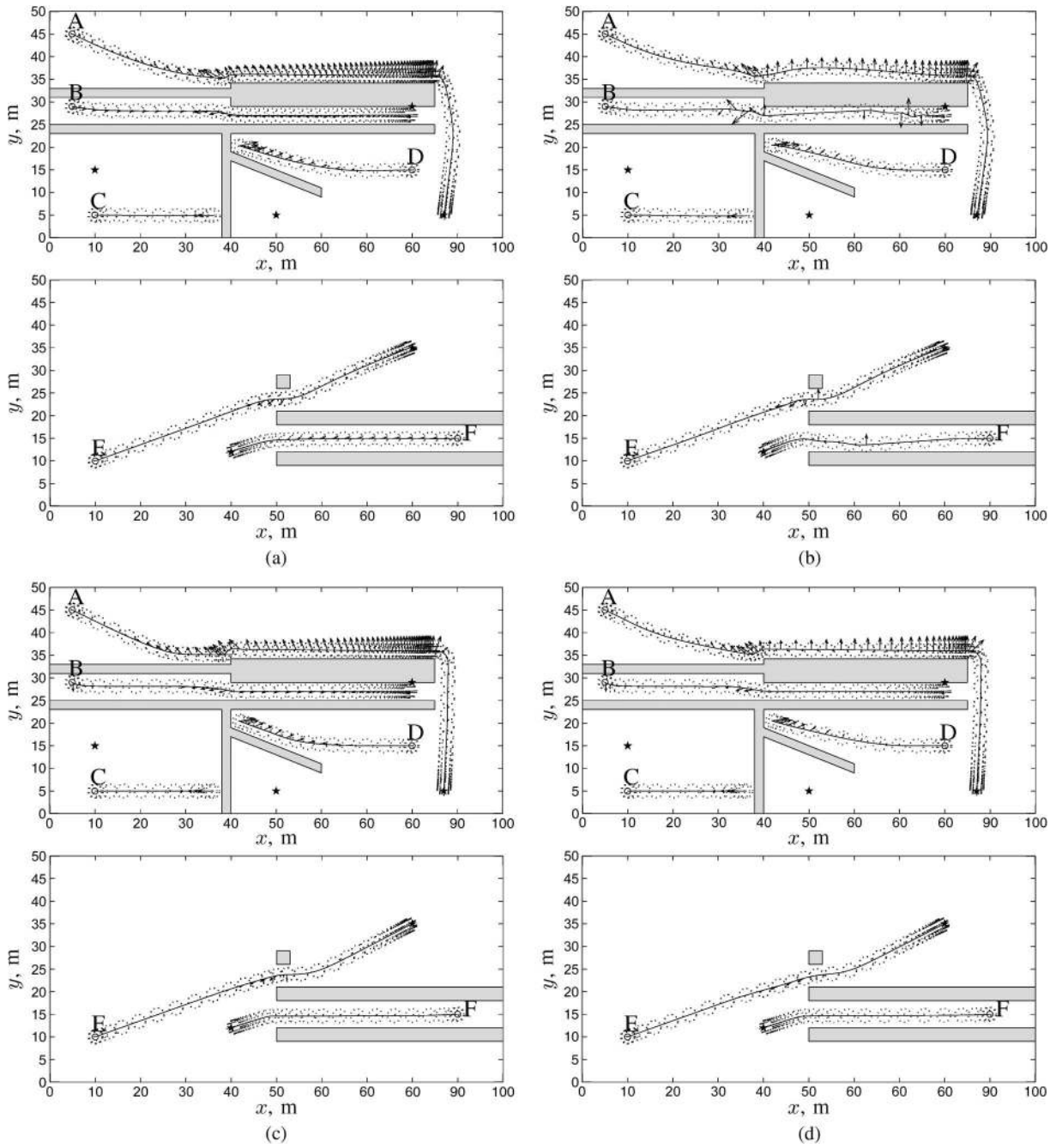

Fig. 12. UAV trajectories with the closed-loop autonomous system using the BRF ($a_{\max} = 1$ m/s^2; $G = 0.1$ s) and the PRF ($a_{\max} = 1$ m/s^2; $d_{\min} = 1.5$ m $(= r_{\mathrm{pz}})$; $t_{\mathrm{ahead}} = 2$ s). (a) BRF, radial risk vectors. (b) BRF, normal risk vectors. (c) PRF, radial risk vectors. (d) PRF, normal risk vectors.

at a larger distance from the obstacle. It can also be seen that, with normal risk vectors, the PRF resulted in high fluctuations in the risk at the corner of the obstacles, whereas the BRF resulted in two rather large peak values.

6) Trajectory F: This trajectory involved a corridor with a width of $4r_{\mathrm{pz}}$ and a target located beyond the bottom wall. It was hypothesized that the UAV would hit the bottom wall of the corridor.

Results show that, with the BRF using normal risk vectors, the vehicle almost hit the bottom wall of the corridor [Fig. 12(b)]. In Section IV-A, it will become clear that the occurrence of a collision depends on the field size. Figs. 13(i) and 14(c) show that the BRF with radial risk vectors resulted in larger risk values and lower UAV velocities than the PRF. Additionally, the BRF with normal risk vectors resulted in two peaks. The first peak occurred when the UAV was about to collide with the wall, and the second one happened at the end of the corridor.

Concluding, the results indicate that, for the BRF, radial projection is more effective to avoid collision in various scenarios. It results in less fluctuations in the risk vectors at corners of obstacles and yields better repulsive information along the direction of motion in narrow corridors. The PRF resulted in smaller repulsive forces than the BRF with the same result, and,

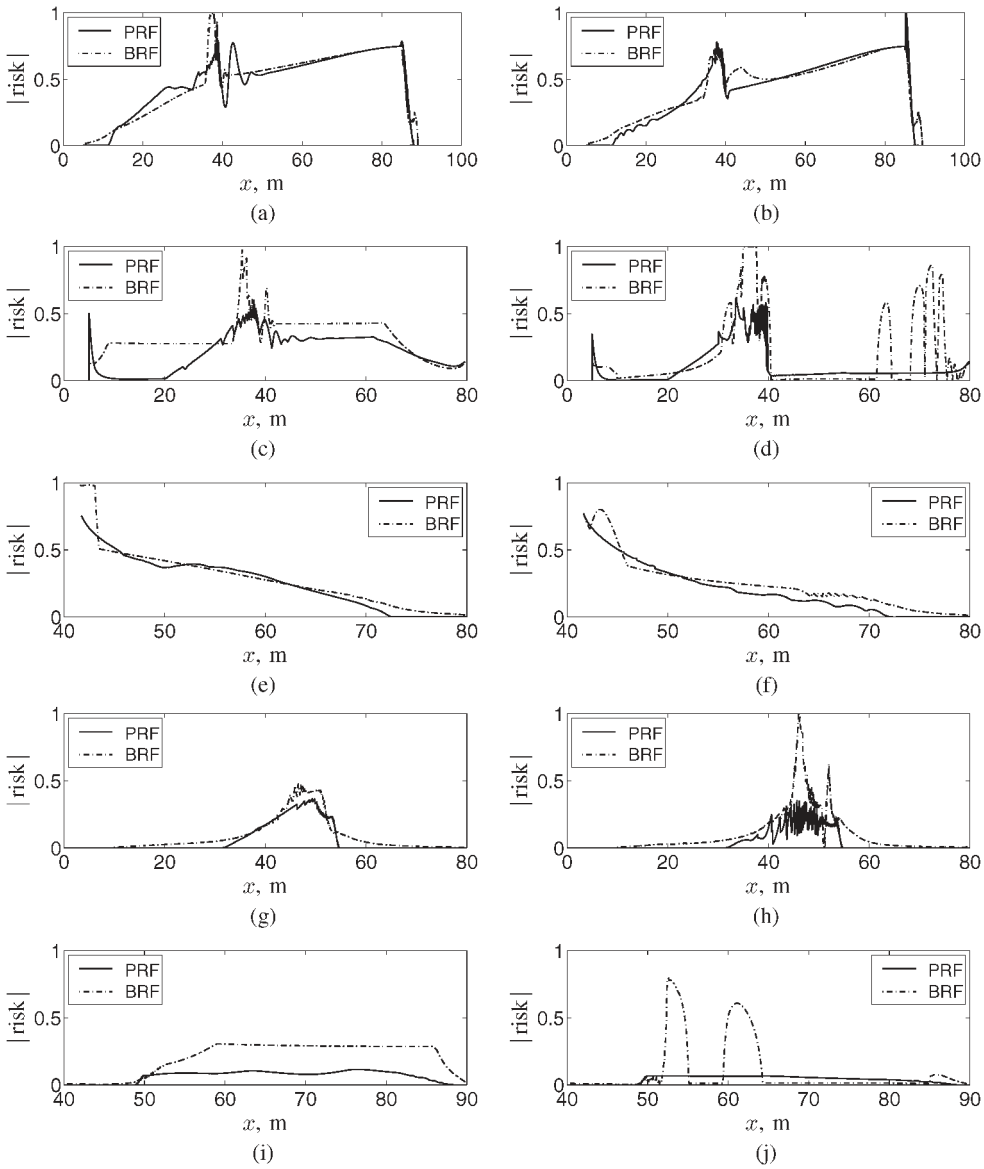

Fig. 13. Magnitude of the total risk vector. BRF: $a_{\max} = 1\ \mathrm{m/s^2}$; $G = 0.1$ s. PRF: $a_{\max} = 1\ \mathrm{m/s^2}$; $d_{\min} = 1.5\ \mathrm{m}\ (= r_{\mathrm{pz}})$; $t_{\mathrm{ahead}} = 2$ s. (a) Trajectory A, radial projection. (b) Trajectory A, normal projection. (c) Trajectory B, radial projection. (d) Trajectory B, normal projection. (e) Trajectory D, radial projection. (f) Trajectory D, normal projection. (g) Trajectory E, radial projection. (h) Trajectory E, normal projection. (i) Trajectory F, radial projection. (j) Trajectory F, normal projection.

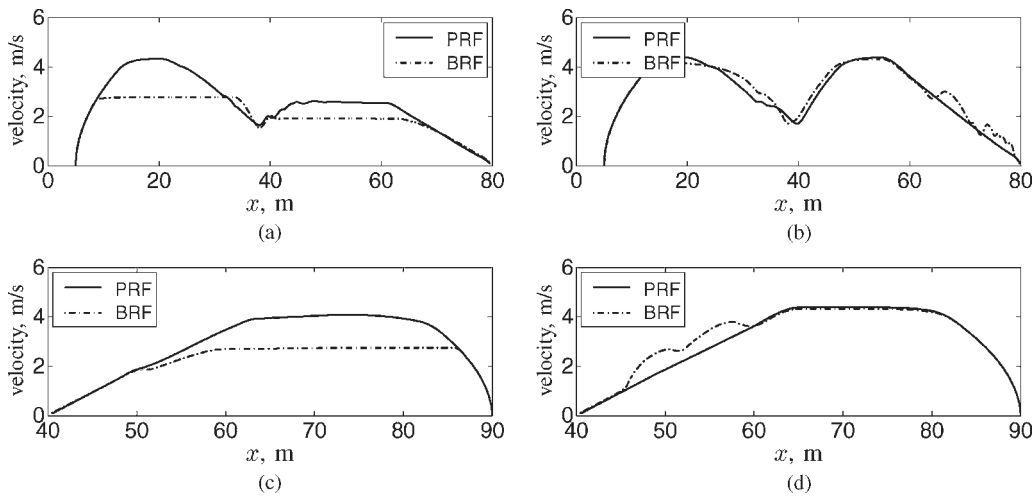

Fig. 14. Velocity of the UAV. BRF: $a_{\max} = 1\ \mathrm{m/s^2}$; $G = 0.1$ s. PRF: $a_{\max} = 1\ \mathrm{m/s^2}$; $d_{\min} = 1.5\ \mathrm{m}\ (= r_{\mathrm{pz}})$; $t_{\mathrm{ahead}} = 2$ s. (a) Trajectory B, radial projection. (b) Trajectory B, normal projection. (c) Trajectory F, radial projection. (d) Trajectory F, normal projection.

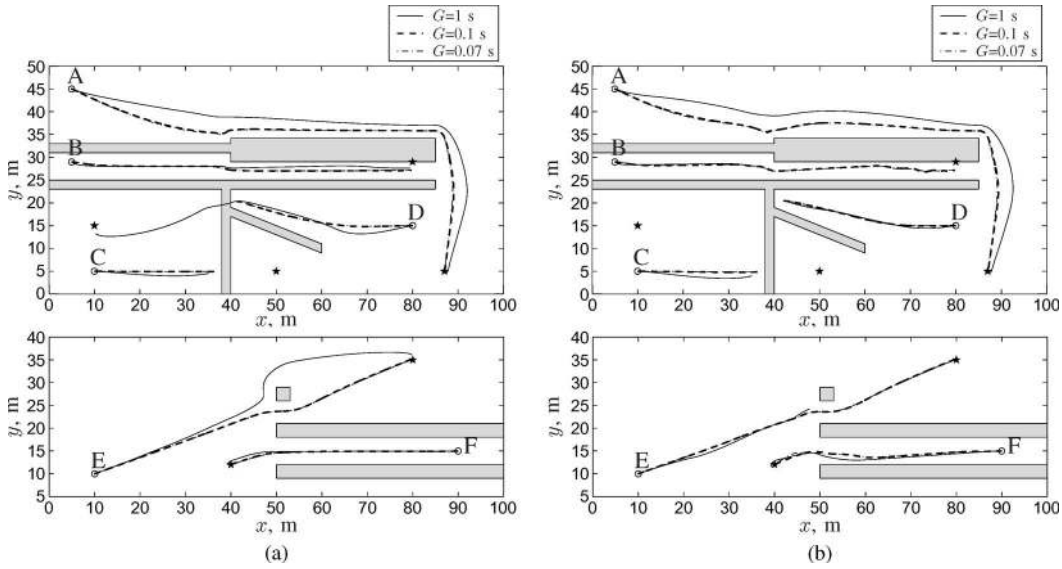

Fig. 15. Simulation results with the BRF for three values of G (1, 0.1, and 0.07 s). The lines represent the traveled path of the UAV for various parameter settings. (a) BRF, radial risk vectors. (b) BRF, normal risk vectors.

therefore, the PRF could be more suitable for haptic feedback, particularly in tasks that require the UAV to move through a narrow corridor. The PRF results were also less dependent on whether normal or radial projection was used.

IV. Parameter Sensitivity Analysis

The simulations in the previous section were conducted with fixed parameter settings. It is important to investigate the effects of changing these parameters on collision avoidance effectiveness and to explore the range of the parameter values that can be selected for tuning the field. Hence, this section first discusses the influence of the scale factor G on the effectiveness of the BRF, followed by a similar analysis for the parameters of the PRF. The sensitivity analysis was done for the same trajectories introduced in Section III.

A. Influence of G on the Effectiveness of the BRF

The influence of G on the effectiveness of the BRF is evaluated by using three values: $G = 0.07$ s, $G = 0.1$ s (as in Section III), and $G = 1$ s. Choosing $G \leq 0.07$ s results in a field that would be too small, unable to effectively assist in collision avoidance in a dead end. On the other hand, taking $G \geq 1$ s leads to a field that would be much too large for narrow corridors, and, as will be discussed in detail next, force field cancellation effects will occur. Fig. 15(a) and (b) shows the simulation results of the BRF with radial and normal risk vectors, respectively.

In trajectory A, the traveled path for $G = 1$ s was further away from the wall, caused by the larger field size. Between $G = 0.1$ s and $G = 0.07$ s, the differences in the path traveled were very small.

In trajectory B, the large field with $G = 1$ s using radial risk vectors caused collision with the narrow corridor. This can be attributed to the fact that the large field covered a substantial part of the upper and lower walls, leading to "cancellation effects" of the risk vectors acting on the UAV from the opposing walls. Fig. 16(b) illustrates that the total risk vector pointed to the left, resulting in just a deceleration and not an avoidance of the steplike change in the wall. Apparently, the sum of the virtual forces that pushed the UAV away from the top wall was more or less the same as the sum of the virtual forces that pushed the UAV away from the bottom wall. The small field [$G = 0.1$ s, Fig. 16(a)] was more suitable for the narrow corridor since the total risk vector was also pointing downward. Hence, it is clear that the field size should match the distance between obstacles, an important design constraint. For the BRF with normal risk vectors, a collision always occurred, independently of the value of G.

In trajectory C, a small deviation of the path in the negative y-direction occurred with $G = 1$ s. Due to the size of the field, the wall on the left of the trajectory was mapped to risk vectors. However, the UAV succeeded to stop in front of the wall blocking the trajectory.

In trajectory D, a collision occurred with the large field ($G = 1$ s) using radial risk vectors. Fig. 16(d) shows that the large field covered a considerable part of the dead-end wall but also the parts of the walls *behind* the UAV. This resulted in cancellation effects of the repulsive forces from the opposing walls and the dead-end wall. With the small field [Fig. 16(c)], the UAV was mainly subjected to the repulsive forces from the dead-end wall, resulting in a more effective deceleration of the UAV.

In trajectory E, with $G = 1$ s and using normal risk vectors, the UAV stopped in front of the passage. The deceleration direction of the vehicle strongly depends on the obstacle surface. Here, it was mainly a deceleration to the left due to the vertical walls [see Fig. 16(f)]. In the case of radial projection [Fig. 16(e)], the UAV moved *around* the little square obstacle with $G = 1$ s. Here, the risk vectors were pointing from the obstacle surface along the sensor radial line toward the vehicle. Therefore, the vehicle was mainly decelerated in a direction that depends on the relative position, size, and density of the obstacles.

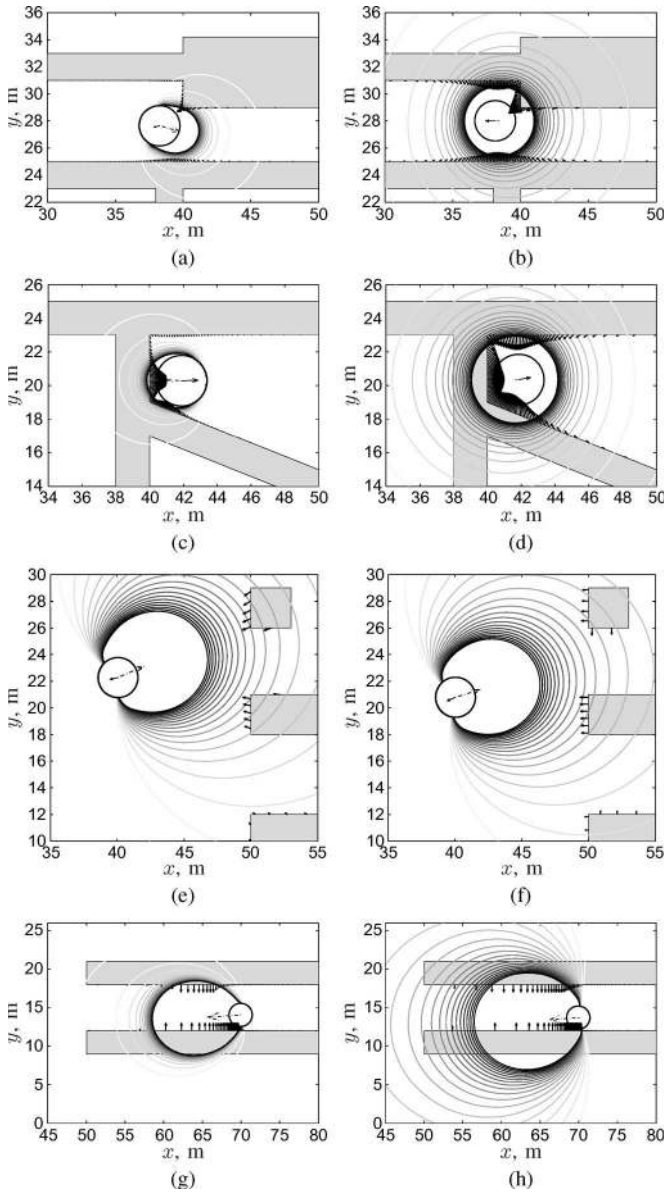

Fig. 16. Close-up of some trajectories with BRF contour lines (all with radial projection unless other specified). (a) Trajectory B, $G = 0.1$ s. (b) Trajectory B, $G = 1$ s. (c) Trajectory D, $G = 0.1$ s. (d) Trajectory D, $G = 1$ s. (e) Trajectory E, $G = 1$ s. (f) Trajectory E, $G = 1$ s, normal projection. (g) Trajectory F, $G = 0.1$ s, normal projection. (h) Trajectory F, $G = 1$ s, normal projection.

In trajectory F, for the BRF with $G = 1$ s and using normal risk vectors, a collision occurred [see Fig. 16(h)]. Again, the large field size resulted in cancellation effects of the individual repulsive forces. The total force became too small to overcome the simulated pilot control actions; the UAV approached the wall too closely and collided.

B. *Influence of $d_{\min}$ and t_{ahead} on the Effectiveness of the PRF*

This section will discuss the influence of $d_{\min}$ and t_{ahead} on the effectiveness of the PRF. First, t_{ahead} is fixed at 2 s, and three values for $d_{\min}$ were used: $0.8r_{\text{pz}}$, $1r_{\text{pz}}$ (as in Section III), and $3r_{\text{pz}}$. Choosing $d_{\min} \leq 0.8r_{\text{pz}}$ results in such a small field that it becomes difficult to avoid rapid changes in the building walls. Taking $d_{\min} \geq 3r_{\text{pz}}$ would result in a field that is too large for narrow passages and dead ends. Fig. 17(a) and (b) shows the simulation results of the PRF with radial and normal risk vectors, respectively.

In trajectory A, the traveled path with $d_{\min} = 3r_{\text{pz}}$ was further away from the wall than with the other parameter values, due to the wider field size, which was similar to but smaller than the effect found for the BRF.

Whereas, in trajectory B, the field with radial risk vectors caused a collision with the BRF, the PRF with radial vectors showed no problem at all. When using the PRF with normal vectors, however, the UAV stopped before the step change in the wall for the largest field.

In trajectory C, the UAV moved along a straight line toward the destination and stopped in front of the wall for all AFF configurations. Contrary to the BRF, no effects of the bottom wall of trajectory B were found.

In trajectory D, for $d_{\min} = 3r_{\text{pz}}$ with radial risk vectors, a collision occurred in the dead end. Similarly to the BRF, Fig. 18(a) and (b) shows that, due to the large field size, a considerable part of the dead end was covered by the field, and the repulsive forces caused by the dead-end wall before the UAV were largely cancelled by the forces due to the walls above, below, and even behind the UAV.

In trajectory E, the same trend as with the BRF occurred when normal risk vectors were used, i.e., the UAV stopped in front of the passage for the large field. However, whereas, with the BRF, the UAV moved around the obstacles with radial risk vectors, with the PRF, the UAV indeed succeeded to pass between the obstacles. Fig. 18(c) and (d) shows that the field size for $d_{\min} = 3r_{\text{pz}}$ was smaller than that of the BRF with $G = 1$ s [compare with Fig. 16(e) and (f)] and, therefore, here, the UAV was subjected to smaller repulsive risk vectors. For the radial risk vectors, the UAV was better able to approach the passage instead of deviating around the little square obstacle. Hence, the PRF is more suitable to move through a set of surrounding obstacles.

No significant differences were found in trajectory F.

Regarding the influence of t_{ahead}, only the marginal differences in the UAV motion were found for three values: 0, 2, and 6 s (with $d_{\min}$ set at $1r_{\text{pz}}$). The maximum value, $t_{\text{ahead}} = 6$ s, resulted in a field length that was somewhat smaller than 50 m, the artificial sensor range.

The main difference caused by the various settings of t_{ahead} was that the UAV started to initiate an avoidance maneuver earlier when t_{ahead} increased. For example, when approaching the straight wall in trajectory D, the risk vector was generated later with $t_{\text{ahead}} = 0$ s, but the growth of the risk as the UAV approached the wall was much faster. When using force feedback to a human operator, one would start sensing the information rather late and may not have enough time to initiate an avoidance maneuver before the force feedback provides the maximum value. This, in turn, could result in large fluctuations in haptic forces, which may lead to high workload. On the other hand, when using a too large t_{ahead}, the risk would be generated in a too early state, such as with the BRF, which is also likely to contribute to workload. Clearly, human-in-the-loop experiments are needed to resolve this issue.

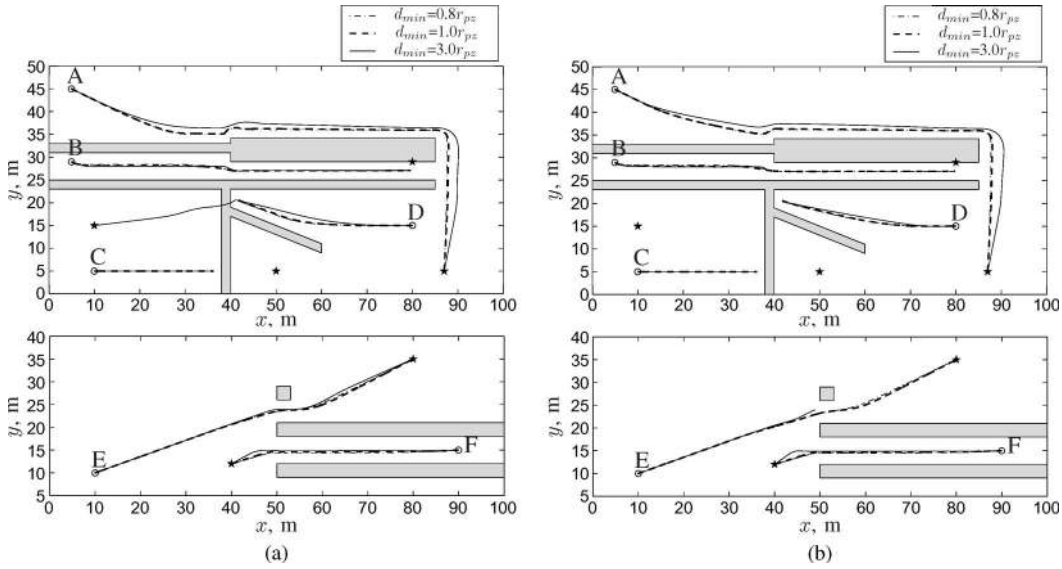

Fig. 17. Simulation results with the PRF for three values of $d_{\min}$ ($0.8r_{\mathrm{pz}}$, $1r_{\mathrm{pz}}$, and $3r_{\mathrm{pz}}$; $t_{\mathrm{ahead}} = 2$ s). The lines represent the traveled path of the UAV for various parameter settings. (a) PRF, radial risk vectors. (b) PRF, normal risk vectors.

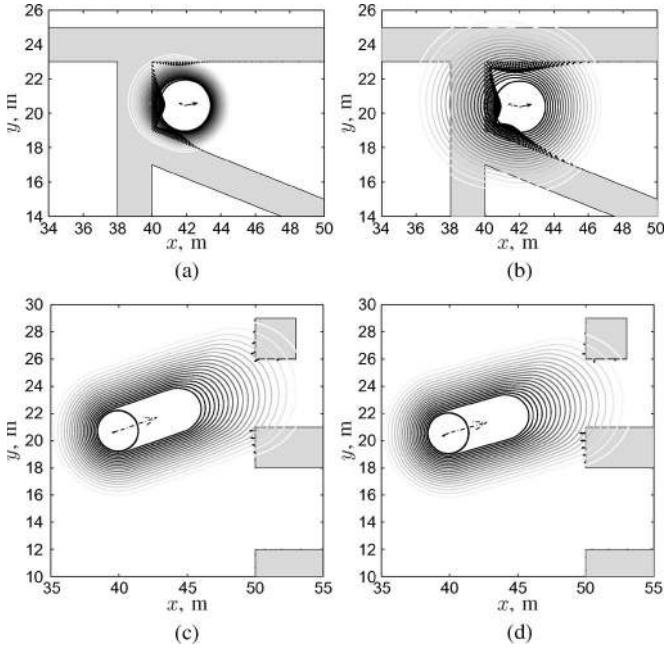

Fig. 18. Close-up of some trajectories with PRF contour lines (all with radial projection unless other specified). (a) Trajectory D, $d_{\min} = r_{\mathrm{pz}}$. (b) Trajectory D, $d_{\min} = 3r_{\mathrm{pz}}$. (c) Trajectory E, $d_{\min} = r_{\mathrm{pz}}$. (d) Trajectory E, $d_{\min} = 3r_{\mathrm{pz}}$, normal projection.

V. Discussion

The parameter sensitivity study showed that neither collisions occurred with the smallest field settings (BRF with $G = 0.07$ s; PRF with $d_{\min} = 0.8r_{\mathrm{pz}}$ and $t_{\mathrm{ahead}} = 2$ s) nor with the initial field settings in Section III (BRF with $G = 0.1$ s; PRF with $d_{\min} = r_{\mathrm{pz}}$ and $t_{\mathrm{ahead}} = 2$ s). The only exception occurred when flying through a narrow corridor (trajectory B) using the BRF with normal risk factors, in which case the UAV always collided.

The sensitivity study revealed that, when the settings are such that the potential field becomes larger, more collisions occur. Table I summarizes the results for the largest field settings (BRF with $G = 1$ s; PRF with $d_{\min} = 3r_{\mathrm{pz}}$ and $t_{\mathrm{ahead}} = 2$ s). From this table, one can see that, generally, the PRF resulted in the best collision avoidance performance. Only with trajectory D a collision occurred, with radial risk vectors. The UAV stopped in front of an obstacle on two occasions (trajectories B and E) with normal risk vectors, but no collisions happened with this particular field.

Trajectories C, D, and E involved situations where, assuming only a forward-looking camera mounted on the vehicle, a human operator would, in principle, be able to *see* the obstacle. Here, the UAV moves toward the obstacle, and the UAV motion is aligned with the camera FOV. The fact that the UAV stops with the automated system used in these simulations is, therefore, of less concern, as, in real applications, the operator "sees" what is happening and can act accordingly. Hence, the collision in trajectory D would probably not happen in real life and is perhaps an artifact of using a rather simple autonomous control system.

In this respect, haptic feedback plays an important role in complementing visual feedback particularly with trajectories A, B, and F. Here, the UAV moves *along* the obstacle walls, and the camera FOV would limit the visibility of the walls near the left and right sides of the UAV. Since no collisions occurred with the PRF in these situations, whereas the BRF resulted in three collisions, it can be concluded that the PRF would be preferred.

Other reasons why the PRF is preferred are that the repulsive risk vector is, generally, smaller than the one generated by the BRF, particularly in situations with many obstacles or in a narrow corridor. Furthermore, the repulsive risk vectors are generated when the vehicle is closer to the obstacles with the PRF. When using haptic feedback, the early generation of rather large repulsive forces could lead to higher operator workload.

With radial projection, the risk vector direction mainly depends on the location, size, and density of the obstacles and less on the surface orientation. This makes the radial risk vectors easier to calculate from the sensor data and more robust in the

TABLE I
SUMMARY OF THE RESULTS FROM THE SENSITIVITY ANALYSIS (LARGEST FIELDS ONLY)

		A	B	C	D	E	F
BRF[1]	radial	pushed away	**collision**	pushed away	**collision**	moves around	·
	normal	pushed away	**collision**	pushed away	·	UAV stops	**collision**
PRF[2]	radial	pushed away	·	·	**collision**	·	·
	normal	pushed away	UAV stops	·	·	UAV stops	·

[1] $G = 1$ s; [2] $d_{min} = 3r_{pz}$, $t_{ahead} = 2$ s

presence of complex-shaped obstacles. The simulation results show that, with the PRF, both normal and radial risk vectors lead to acceptable results (see Table I).

For a scenario with obstacles at one side of the UAV and when the task does not require a close approach, the BRF with either radial or normal projection would be recommended. The large field provides a safe distance from the obstacle. For a scenario with closely spaced obstacles or a narrow passage, however, the PRF with radial projection would be recommended. The smaller and tubelike size allows a better approach toward and through a passage. Radial projection also yields better haptic information about the location of the closely spaced obstacles.

Note that, in this study, the risk was converted into a repulsive haptic feedback signal by a gain of one and, hence, the repulsive force was the same as the risk. For manual teleoperation, a different gain can be selected in order to provide haptic feedback to the human operator such that she or he would be able to perceive the repulsive forces on top of the usual mass–spring–damper dynamics of the control manipulator. Due to the fact that the risk value is limited, the repulsive force will also be limited, and, thus, it will not lead to excessive physical workload or injuries.

VI. RECOMMENDATIONS

In this paper, the human pilot was simulated with a simple controller that generates a control signal that intends to bring the UAV to a certain goal position. Superimposed to this control signal is the control signal calculated from the potential field. The risk field and the gain, with which the risk field result value is weighed in the total control response, were tuned until a desirable performance was found. The simulations showed that, even in the presence of a drive toward a goal position, the avoidance vector generated by the risk field is effective in avoiding collisions. Despite this success, the current study has some important limitations that need to be addressed.

First of all, as the second stage in haptic feedback design, the haptic interface still needs to be designed. That is, the risk field output must be presented as a haptic input signal on the operator's control device. An obvious choice would be to convert the risk value into an additional force on the stick. The stick movement and, therefore, the input to the UAV would then be the result of the forces exerted by the human pilot and those of the haptic feedback. The proper tuning of the haptic "display" is a difficult problem. With operators holding the control manipulator, the effects of the haptic feedback depend on the neuromuscular system dynamics, which are likely to include adaptive reflexive behavior [28], [35]–[38]. For instance, the neuromuscular stiffness is not fixed but changes due to the settings of the reflexive feedback gains, the characteristics of which, in turn, depend on, among others, the task being conducted, and the bandwidth of external disturbances [39], [40]. In a follow-up paper, the issues involved in tuning the haptic feedback for UAV teleoperation, taking in particular the dynamics of the human neuromuscular system into account, will be dealt with in detail [25].

When an appropriate setting has been found, human-in-the-loop experiments with a human operator controlling the UAV need to be conducted [41]. Clearly, more insight needs to be gained into how the various tuning parameters of the haptic feedback, including those related to the AFF as discussed in this paper, have an effect on operator performance, situation awareness, control activity, and workload. Preliminary studies have indicated that the PRF described in this paper indeed performed very well [27], [28], [41].

A further recommendation would be to investigate in what ways the risk can "haptically" be presented to a human operator. Aside from the most obvious implementation mentioned previously—presenting the risk through a force offset on the stick—an alternative would be by means of an increase in the spring constant of the manipulator dynamics, i.e., changing the stiffness of the manipulator as a function of the risk [28], [40], [42]. Such novel ways of haptic presentation, when carefully tuned to the constraints imposed by the operator and the environment, in principle, allow for "sharing control" between the automation—implemented through the collision avoidance function in this paper—and the human operator [40], [43]–[46]. Here, dependent on the force feedback or stiffness feedback gain, control is, quite literally, shared between man and machine, and both work alongside to effectively achieve the task performance and safety goals [28]. Additionally, by presenting the level of shared control through haptic feedback, the human internal representation of the shared control system could be improved. Poncela *et al.* [47] developed a shared control system without haptic feedback and found that subjects were unable to determine when they had more help from the automation.

Finally, the effects of time delays and sensor inaccuracies need to be investigated. In this respect, Lam *et al.* [27] showed that the effects of signal transmission delays up to 400 ms, potentially very harmful for the high-bandwidth haptic feedback loop, can effectively be resolved through adopting the "wave variables" transformation developed by Niemeyer and Slotine [48], [49]. Effects of sensor inaccuracies, such as effects of resolution, remain to be investigated, however. Neglected in this study, these inaccuracies are likely to result

in small irregular haptic force variations that are difficult to interpret by operators, hard to act upon, and therefore likely to contribute to workload [40].

VII. Conclusion

Regarding the AFF representations, the PRF is preferred over the BRF for collision avoidance in an autonomous UAV helicopter control. With the PRF, the repulsive forces are smaller, they build up later, and allow for higher UAV velocities. With the PRF, both normal and radial risk vectors can be used. It is found that, generally, parameter settings that result in smaller fields, that is, measured relative to the dimensions of obstacles, yield better performance. Surprisingly, larger fields lead to *more* collisions because of "force cancellation effects." Here, the repulsive forces that emerge from various obstacles around the vehicle "add up" to an almost zero total risk, and therefore no feedback at all.

This study further showed that a "good" field size depends on the characteristics of the world, like the size of passages between obstacles relative to the size of the vehicle, but also on what one wants to do with the UAV, i.e., enter the corridor or simply stay away from it. A tradeoff between safety and operational needs is inevitable.

Future research will involve the design and tuning of the haptic interface, including human-in-the-loop experiments to evaluate its effects on operator workload and situation awareness.

References

[1] C. B. Monson, C. S. Fong, R. A. Marsh, and M. W. Haas, "Addressing the human element in unmanned aerial vehicles," in *Proc. 36th Aerosp. Sci. Meeting Exhib.*, Reno, NV, Jan. 12–15, 1998, pp. 1–7.

[2] J. S. McCarley and C. D. Wickens, "Human factors implications of UAVs in the national airspace," Aviation Human Factors Division, Savoy, IL, Tech. Rep. AHFD-05-05/FAA-05-01, 2005.

[3] N. Diolaiti and C. Melchiorri, "Tele-operation of a mobile robot through haptic feedback," in *Proc. IEEE Int. Workshop HAVE*, Ottawa, ON, Canada, Nov. 17–18, 2002, pp. 67–72.

[4] S. Lee, G. S. Sukhatme, G. J. Kim, and C. Park, "Haptic control of a mobile robot: A user study," in *Proc. IEEE/RSJ Int. Conf. Intell. Robots Syst.*, Lausanne, Switzerland, 2002, vol. 3, pp. 2867–2874.

[5] D. Xiao and R. Hubbold, "Navigation guided by artificial force fields," in *Proc. Conf. Human Factors Comput. Syst.*, Los Angeles, CA, Apr. 18–23, 1998, pp. 179–186.

[6] I. Elhajj, N. Xi, W. K. Fung, Y. H. Liu, W. J. Li, T. Kaga, and T. Fukuda, "Haptic information in Internet-based teleoperation," *IEEE/ASME Trans. Mechatronics*, vol. 6, no. 3, pp. 295–304, Sep. 2001.

[7] D. W. Repperger, A. P. Chandler, and T. L. Chelette, "A study on spatially induced "virtual force" with an information theoretic investigation of human performance," *IEEE Trans. Syst., Man, Cybern.*, vol. 25, no. 10, pp. 1392–1404, Oct. 1995.

[8] B. Hannaford, L. P. Wood, D. A. McAffee, and H. Zak, "Performance evaluated of a six-axis generalized force-reflecting teleoperator," *IEEE Trans. Syst., Man, Cybern.*, vol. 21, no. 3, pp. 620–633, May/Jun. 1991.

[9] F. Huang, R. B. Gillespie, and A. Kuo, "Haptic feedback and human performance in a dynamic task," in *Proc. 10th Symp. Haptic Interfaces Virtual Environ. Teleoperator Syst.*, Orlando, FL, Mar. 24–25, 2002, pp. 24–31.

[10] D. W. Repperger, "Active force reflection devices in teleoperation," *IEEE Control Syst. Mag.*, vol. 11, no. 1, pp. 52–56, Jan. 1991.

[11] J. Borenstein and Y. Koren, "Real-time obstacle avoidance for fast mobile robots," *IEEE Trans. Syst., Man, Cybern.*, vol. 19, no. 5, pp. 1179–1187, Sep. 1989.

[12] S. Hong, J. Lee, and S. Kim, "Generating artificial force for feedback control of teleoperated mobile robots," in *Proc. IEEE/RSJ Int. Conf. Intell. Robots Syst.*, Kyongju, South Korea, Oct. 17–21, 1999, vol. 3, pp. 1721–1726.

[13] O. Khatib, "Real-time obstacle avoidance for manipulators and mobile robots," *Int. J. Robot. Res.*, vol. 5, no. 1, pp. 90–98, 1986.

[14] B. H. Krogh, "A generalized potential field approach to obstacle avoidance control," Soc. Manuf. Eng., Dearborn, MI, Tech. Paper MS84-484, 1984.

[15] T. Arai, H. Ogata, and T. Suzuki, "Collision avoidance among multiple robots using virtual impedance," in *Proc. IEEE/RSJ Int. Workshop Intell. Robots Syst.*, Tsukuba, Japan, Sep. 4–6, 1989, pp. 479–485.

[16] N. Hogan, "Impedance control: An approach to manipulation: Part III—Applications," *Trans. ASME, J. Dyn. Meas. Control*, vol. 107, no. 1, pp. 17–24, Mar. 1985.

[17] A. A. Masoud, "Decentralized self-organizing potential field-based control for individually motivated mobile agents in a cluttered environment: A vector-harmonic potential field approach," *IEEE Trans. Syst., Man, Cybern. A, Syst., Humans*, vol. 37, no. 3, pp. 372–390, May 2007.

[18] E. Rimon and D. E. Koditschek, "Exact robot navigation using artificial potential functions," *IEEE Trans. Robot. Autom.*, vol. 8, no. 5, pp. 501–518, Oct. 1992.

[19] R. Volpe and P. K. Khosla, "Manipulator control with superquadric artificial potential functions: Theory and experiments," *IEEE Trans. Syst., Man, Cybern.*, vol. 20, no. 6, pp. 1423–1436, Nov./Dec. 1990.

[20] J. Kim and P. K. Khosla, "Real-time obstacle avoidance using harmonic potential functions," *IEEE Trans. Robot. Autom.*, vol. 8, no. 3, pp. 338–349, Jun. 1992.

[21] D. H. Kim and S. Shin, "Local path planning using a new artificial potential function composition and its analytical design guidelines," *Adv. Robot.*, vol. 20, no. 1, pp. 115–135, 2006.

[22] W. H. Huang, B. R. Fajen, J. R. Fink, and W. H. Warren, "Visual navigation and obstacle avoidance using a steering potential function," *Robot. Auton. Syst.*, vol. 54, no. 4, pp. 288–299, Apr. 2006.

[23] J. Borenstein and Y. Koren, "The vector field histogram—Fast obstacle avoidance for mobile robots," *IEEE J. Robot. Autom.*, vol. 7, no. 3, pp. 278–288, Jun. 1989.

[24] D. Fox, W. Burgard, and S. Thrun, "The dynamic window approach to collision avoidance," *IEEE Robot. Autom. Mag.*, vol. 4, no. 1, pp. 23–33, Mar. 1997.

[25] M. M. van Paassen, J. Lasschuit, T. M. Lam, M. Mulder, and D. A. Abbink, "Tuning of haptic feedback for UAV tele-operation," *IEEE Trans. Syst., Man, Cybern.*, to be published.

[26] G. M. Voorsluijs, S. Bennani, and C. W. Scherer, "Linear and parameter-dependent robust control techniques applied to a helicopter UAV," in *Proc. 38th AIAA Guidance, Navig. Control Conf.*, Providence, RI, Aug. 16–19, 2004, pp. 1–11.

[27] T. M. Lam, M. Mulder, and M. M. Van Paassen, "Haptic feedback in uninhabited aerial vehicle teleoperation with time delay," *J. Guid. Control Dyn.*, vol. 31, no. 6, pp. 1728–1739, 2008.

[28] T. M. Lam, M. Mulder, M. M. van Paassen, J. A. Mulder, and F. C. T. van der Helm, "Force-stiffness feedback in uninhabited aerial vehicle teleoperation with time delay," *AIAA J. Guid. Control Dyn.*, vol. 32, no. 3, pp. 821–835, 2009.

[29] P. K. Egbert and S. H. Winkler, "Collision-free object movement using vector fields," *IEEE Comput. Graph. Appl.*, vol. 16, no. 4, pp. 18–24, Jul. 1996.

[30] S. S. Ge and Y. J. Cui, "Dynamic motion planning for mobile robots using potential field method," *Auton. Robots*, vol. 13, no. 3, pp. 207–222, Nov. 2002.

[31] J. Minguez, L. Montano, and O. Khatib, "Reactive collision avoidance for navigation with dynamic constraints," in *Proc. IEEE/RSJ Int. Conf. Intell. Robots Syst.*, Lausanne, Switzerland, Oct. 2002, pp. 588–594.

[32] A. Poty, P. Melchior, and A. Oustaloup, "Dynamic path planning for mobile robots using fractional potential field," in *Proc. 1st Int. Symp. Control, Commun. Signal Process.*, Hammamet, Tunisia, Mar. 21–24, 2004, pp. 557–561.

[33] H. W. Boschloo, T. M. Lam, M. Mulder, and M. M. Van Paassen, "Collision avoidance for a remotely-operated helicopter using haptic feedback," in *Proc. IEEE Int. Conf. Syst., Man, Cybern.*, The Hague, The Netherlands, Oct. 10–13, 2004, pp. 229–235.

[34] Y. Koren and J. Borenstein, "Potential field methods and their inherent limitations for mobile robot navigation," in *Proc. IEEE Conf. Robot. Autom.*, Sacramento, CA, Apr. 9–11, 1991, pp. 1398–1404.

[35] E. de Vlugt, A. C. Schouten, and F. C. T. van der Helm, "Closed-loop multivariable system identification for the characterization of the dynamic arm compliance using continuous force disturbances: A model study," *J. Neurosci. Methods*, vol. 122, no. 2, pp. 123–140, Jan. 2003.

[36] E. De Vlugt, "Identification of spinal reflexes," Ph.D. dissertation, Faculty Des., Eng. Prod., Delft Univ. Technol., Delft, The Netherlands, 2004.

[37] A. C. Schouten, "Proprioceptive reflexes and neurological disorders," Ph.D. dissertation, Faculty Des., Eng. Prod., Delft Univ. Technol., Delft, The Netherlands, 2004.
[38] D. A. Abbink, "Biomechanical analysis of drivers during haptic feedback," Ph.D. dissertation, Faculty Aerosp. Eng., Delft Univ. Technol., Delft, The Netherlands, 2006.
[39] M. Mulder, "Haptic gas pedal feedback for active car-following support," Ph.D. dissertation, Faculty Aerosp. Eng., Delft Univ. Technol., Delft, The Netherlands, 2006.
[40] D. A. Abbink and M. Mulder, "Exploring the dimensions of haptic feedback support in manual control," *J. Comput. Inf. Sci. Eng.*, vol. 9, no. 1, p. 011 006, Mar. 2009.
[41] T. M. Lam, M. Mulder, and M. M. Van Paassen, "Haptic interface for UAV collision avoidance," *Int. J. Aviation Psychol.*, vol. 17, no. 2, pp. 45–73, Apr. 2007.
[42] T. M. Lam, M. Mulder, and M. M. Van Paassen, "Haptic feedback for UAV tele-operation—Force offset and spring load modification," in *Proc. IEEE Int. Conf. Syst., Man, Cybern.*, Taipei, Taiwan, Oct. 8–11, 2006, pp. 1618–1623.
[43] M. Steele and R. B. Gillespie, "Shared control between human and machine: Using a haptic steering wheel to aid in land vehicle guidance," in *Proc. 45th Annu. Meeting Human Factors Ergonomics Soc.*, Minneapolis, MN, Oct. 8–2, 2001, pp. 1671–1675.
[44] P. Griffiths and R. B. Gillespie, "Sharing control between human and automation using haptic interface: Primary and secondary task performance benefits," *Hum. Factors*, vol. 47, no. 3, pp. 574–590, 2005.
[45] M. K. O'Malley, A. Gupta, M. Gen, and Y. Li, "Shared control in haptic systems for performance enhancement and training," *Trans. ASME, J. Dyn. Syst. Meas. Control*, vol. 128, no. 1, pp. 75–85, Mar. 2006.
[46] M. Mulder, D. A. Abbink, and E. R. Boer, "The effect of haptic guidance on curve negotiation behavior of young, experienced drivers," in *Proc. IEEE-SMC*, Singapore, Oct. 12–15, 2008.
[47] A. Poncela, C. Urdiales, E. J. Pérez, and F. Sandoval, "A new efficiency-weighted strategy for continuous human/robot cooperation in navigation," *IEEE Trans. Syst., Man, Cybern. A, Syst., Humans*, vol. 39, no. 3, pp. 486–499, May 2009.
[48] G. Niemeyer, "Using wave variables in time delayed force reflecting teleoperation," Ph.D. dissertation, MIT, Cambridge, MA, 1996.
[49] G. Niemeyer and J. J. E. Slotine, "Telemanipulation with time delays," *Int. J. Robot. Res.*, vol. 23, no. 9, pp. 873–890, Sep. 2004.

Thanh Mung Lam received the M.Sc. degree in aerospace engineering from the Delft University of Technology (TU Delft), Delft, The Netherlands, in 2003, with a thesis on comparative study between control and display augmentation techniques for tunnel-in-the-sky displays, where he is currently working toward the Ph.D. degree in aerospace engineering, with a thesis on haptic interface for teleoperation of uninhabited aerial vehicles.

He is currently a Software Engineer with Moog, Nieuw-Vennep, The Netherlands, where he is developing real-time software controllers for hexapods.

Mr. Lam was the recipient of the 2007 Franklin V. Taylor Memorial Award for the best paper published in the 2006 IEEE Systems, Man, and Cybernetics conference proceedings, where he coauthored with M. Mulder and M. M. (René) van Paassen.

Harmen Wigert Boschloo received the M.Sc. degree in aerospace engineering from the Delft University of Technology (TU Delft), Delft, The Netherlands, in 2004. He worked for a year at the Department of Biomechanical Engineering in the Delft University of Technology.

Thereafter he moved to the Aerospace Software and Technologies Institute, TU Delft, as a Software and Research Engineer. His interests include software development, game development, artificial intelligence, simulation, and human–machine interaction.

Max Mulder received the M.Sc. and Ph.D. degrees (*cum laude*) in aerospace engineering from the Delft University of Technology (TU Delft), Delft, The Netherlands, in 1992 and 1999, respectively, for his work on cybernetics of tunnel-in-the-sky displays.

He is currently a Full Professor and the Head of the Control and Simulation Division, Faculty of Aerospace Engineering, TU Delft. His research interests include cybernetics and its use in modeling human perception and performance and cognitive systems engineering and its application in the design of "ecological" human–machine interfaces.

Marinus M. (René) van Paassen (M'09) received the M.Sc. degree and the Ph.D. degree, with a thesis on neuromuscular system of the pilot's arm, from the Delft University of Technology (TU Delft), Delft, The Netherlands, in 1988 and 1994, respectively.

He spent two years as a Postdoctoral Fellow (Brite/EuRam Research Fellow) with the University of Kassel, Kassel, Germany, with Prof. Johannsen, where he worked on the development of alternative interfaces for process control based on functional models of the process, and half a year with the Technical University of Denmark, Lyngby, Denmark, where he worked on multilevel flow modeling. He is currently an Associate Professor with the Faculty of Aerospace Engineering, TU Delft, where he is working on aircraft simulation and human–machine interaction, with focus on cybernetics, haptics, and the application of ecological interface design for flight deck and air traffic control displays.